A Microscale Model for Ausferritic Transformation of Austempered Ductile Irons

ADRIÁN D. BOCCARDO, PATRICIA M. DARDATI, DIEGO J. CELENTANO, and LUIS A. GODOY

This paper presents a new metallurgical model for the ausferritic transformation of ductile cast iron. The model allows predicting the evolution of phases in terms of the chemical composition, austenitization and austempering temperatures, graphite nodule count, and distribution of graphite nodule size. The ferrite evolution is predicted according to the displacive growth mechanism. A representative volume element is employed at the microscale to consider the phase distributions, the inhomogeneous austenite carbon content, and the nucleation of ferrite subunits at the graphite nodule surface and at the tips of existing ferrite subunits. The performance of the model is evaluated by comparison with experimental results. The results indicate that the increment of the ausferritic transformation rate, which is caused by increments of austempering temperature and graphite nodule count, is adequately represented by this model.

DOI: 10.1007/s11661-016-3816-9

I. INTRODUCTION

DUCTILE cast iron, also known as nodular cast iron, is a C-Si-Fe-based alloy with a microstructure formed by graphite nodules and a metal matrix. In a continuous cooling process, the resulting matrix could be ferritic, pearlitic, or ferritic-pearlitic, whereas other microstructures, such as ausferritic and martensitic, may be formed by following specific cooling processes.

In austempered ductile iron (ADI), the graphite nodules are embedded in an ausferritic matrix formed by ferrite subunits (lamellae, platelets, or disks) and carbon-rich austenite.[1,2] ADI is employed in several industrial applications, such as the fabrication of shafts, cams, and gears, due to its high strength, wear resistant, adequate fatigue response, and good toughness properties.[3]

The ausferritic matrix is currently obtained by means of two different heat treatments. The first one is a *three-step* heat treatment,[4–7] in which a ductile cast iron is heated from ambient temperature up to the austenitization temperature T_γ in order to obtain a full austenitic matrix with the appropriate carbon content (austenitizing step). Then, the material is suddenly cooled down and kept at the austempering temperature T_A to initiate the austempering process (quenching and austempering steps). The *three-step* heat treatment is used, for example, for ductile cast iron with a ferritic, pearlitic, or ferritic-pearlitic initial matrix.

The second procedure employed in practice is an *in situ* heat treatment,[3,8] in which the austenitizing step is absent because after solidification the material is cooled down and kept at the desired austenitization temperature in order to obtain austenite with an appropriate carbon content. As in the *three-step* heat treatment, the material is then suddenly cooled down and kept at the austempering temperature to initiate the austempering process.

In both heat treatments discussed above, the cooling rate from T_γ to T_A and the chemical composition play a key role. If the cooling rate is not high enough, the reconstructive ferritic and pearlitic transformations are not avoided. In this situation, the hardenability of the ductile cast iron could be improved with the addition of some alloys elements, such as Mn, Mo, and Ni.[7]

The austempering process may be divided in two stages and an interval between them called processing window.[5,6] The stage I begins with the start of the ausferritic transformation and ends when the fraction of ferrite subunits and the austenite carbon content reach their maximum values. During the processing window, the ferrite fraction and austenite carbon content remain constants. The stage II begins, after the processing window, when the carbide precipitation from austenite starts. The extent of the processing window is a function of chemical composition and micro-segregation.

According to the above description, the required matrix is obtained by cooling down the parts up to

ADRIÁN D. BOCCARDO, Ph.D. Student, and PATRICIA M. DARDATI, Professor, are with the Department of Mechanical Engineering-GIDMA, CONICET, Facultad Regional Córdoba, Universidad Tecnológica Nacional, Maestro M. Lopez esq. Cruz Roja Argentina, Córdoba, Argentina. Contact e-mail: aboccardo@mecanica.frc.utn.edu.ar DIEGO J. CELENTANO, Professor, is with the Department of Mechanical and Metallurgical Engineering, Research Center for Nanotechnology and Advanced Materials (CIEN-UC), Pontificia Universidad Católica de Chile, Vicuña Mackenna 4860, Santiago de Chile, Chile. LUIS A. GODOY, Director, is with the Institute for Advanced Studies in Engineering and Technology, FCEFyN, CONICET-Universidad Nacional de Córdoba, Av. Vélez Sarsfield 1611, Córdoba, Argentina.

Manuscript submitted January 15, 2016.

Published online: 20 October 2016

ambient temperature at the end of the ausferritic transformation. With an early cooling, the matrix could contain martensite, meanwhile with a late cooling, the matrix could contain carbide;[9] therefore, the prediction of the phase evolution during the ausferritic transformation is very important in the design of parts.

There are several experimental works about the kinetics of ausferritic transformation. The influence of chemical composition, and austenitizing and austempering temperatures has been studied in References 10, 11, 12, and 13. An important influence of graphite nodule count has been recently reported in Reference 4.

According to physical metallurgy, each ferrite subunit is formed by means of nucleation and growth processes.[14] There are two mechanisms that explain the subunit growth: The displacive mechanism proposes that austenite transforms into a carbon-supersaturated ferrite subunit, without carbon diffusion between these phases. Once the subunit growth stops, the excess of carbon within the subunit is redistributed to the austenite. Moreover, at the end of the ausferritic transformation, the austenite carbon concentration is equal to $c_{\gamma_{T_{0'}}}$. On the other hand, the diffusive mechanism considers that a subunit grows by carbon diffusion through the ferrite-austenite interface, and the austenite carbon concentration, at the end of the transformation, is equal to the paraequilibrium concentration Ae'_3. The displacive mechanism is well accepted to explain this transformation in ADI and bainitic steels.[6,15] There is experimental evidence that support this mechanism, one of them is that the final austenite carbon concentration is close to $c_{\gamma_{T_{0'}}}$ instead of Ae'_3.[9,16,17]

The evolution of phases during the ausferritic transformation has been modeled by different authors. Yoo *et al.*[3] considered the evolution of ausferrite fraction using a model based on Avrami's equation. This approach is not able to predict the volume fractions of ferrite platelets and austenite, so that it becomes difficult to estimate the mechanical properties of ADI. Boccardo *et al.*[5] presented a metallurgical model to predict the volume fraction of ferrite platelets, in which the matrix is formed by ferrite platelets and austenite, both of them with homogeneous carbon content. The phase fractions at the end of the transformation are computed considering the mass conservation into the matrix, and the ferrite evolution is evaluated by Avrami's equation. Thomson *et al.*[6] presented a modified steel model considering a displacive mechanism growth. In this approach, ferrite subunits having a prefixed size nucleate continuously within the austenite with homogeneous carbon content. The nucleation law takes into account the austempering temperature, austenite carbon concentration, and the number of subunits that have already nucleated. Kapturkiewicz *et al.*[1] presented a model considering the diffusive mechanism growth which accounts for continuous nucleation (following Avrami's equation) and growth of ferrite lamellae. The growth model considers only a ferrite lamella embedded into austenite. The lamella is assumed to have an infinite length, and its thickness increases by the unidimensional carbon diffusion through the ferrite-austenite interface.

The models described above have several parameters which need to be fitted using specific experiments. Because these parameters depend on graphite nodule size, chemical composition, and austenitization and austempering temperatures (the last parameter is considered by Thomson's model), the fitting process requires having a large number of experimental results. This fact limits the application of models when new ADI are developed. Furthermore, the output of these models does not provide much information about microstructure features like subunit dimension and austenite carbon concentration.

Thus, it seems that a new model is needed to simulate the ausferritic transformation by taking into account the most important characteristics of the microstructure, in order to improve predictions and simplify the fitting process. This paper presents a new ausferritic model, according to the displacive mechanism growth, which allows predicting the evolution of phases during the first stage of the austempering process of ductile cast iron. Unlike the previously mentioned models, the proposed microscale model considers the effects of graphite nodule size, distribution of graphite nodule size, ferrite subunit size, distribution of phases into the microstructure, and inhomogeneous austenite carbon concentration. The metallurgical model is presented in Section II. The numerical heat treatment and details of the fitting process are included in Section III, and the results are discussed in Section IV. Finally, the concluding remarks are drawn in Section V.

II. METALLURGICAL MODEL

During the ausferritic transformation, the ferrite is formed by nucleation and growth of subunits. Based on the literature review, the displacive mechanism growth provides a suitable explanation to the phenomena and has been assumed in this work. The subunits are formed when the following thermodynamic criteria for both nucleation and growth are, respectively, satisfied[15,18]:

$$\Delta G_m < G_n, \quad [1]$$

$$\Delta G^{\gamma\rightarrow\alpha} < G_{sd}, \quad [2]$$

where ΔG_m is the maximum free energy available for nucleation, G_n is the minimum energy necessary to obtain a detectable amount of ferrite, $\Delta G^{\gamma\rightarrow\alpha}$ is the free energy change for the transformation of austenite into ferrite with the same chemical composition, and G_{sd} is the stored energy due to the shape deformation.

The subunit size is limited by the plastic relaxation in the adjacent austenite.[18] The excess of carbon content within the subunit is rejected to austenite after the subunit growth stops.[6,15,18] The austenite carbon enrichment reduces the magnitude of both ΔG_m and $\Delta G^{\gamma\rightarrow\alpha}$. If the austenite carbon content is high enough, either one or both thermodynamic criteria are not satisfied; therefore, the ausferritic transformation stops. When the austenite carbon content reaches the

concentration $c_{\gamma_{T_{0'}}}$, this model considers that both criteria are not satisfied at the same time.

A. *Representative Volume Element (RVE)*

The proposed metallurgical model considers a spherical RVE to describe the microstructure evolution of a ductile cast iron during the ausferritic transformation, as shown in Figure 1. The graphite nodules are classified in different size sets: A set i is formed by all graphite nodules having radius r_{Gr_i}. Taking into account this graphite nodule classification, each RVE_i is formed by a graphite nodule surrounded by a metallic matrix. At the beginning of the transformation, the matrix is formed by austenite with homogeneous carbon content, whereas during the transformation, the matrix is formed by ferrite and austenite with inhomogeneous carbon content.

This model considers three regions of austenite with different carbon contents: (1) austenite film that forms part of the sheaves, (2) austenite block that is placed between the sheaves, and (3) austenite halo. The average carbon contents of the film, block, and halo are $c_{\gamma_{\mathrm{film}}}$, $c_{\gamma_{\mathrm{block}_i}}$, and $c_{\gamma_{\mathrm{halo}}}$, respectively. The distribution of phases within the RVE_i is defined according to experimental observation. In this model, the austenite film and austenite block, together with the ferrite subunits, form the ausferrite. The ausferrite forms a spherical envelope around the graphite nodule, and its external radius grows during the transformation. The spherical envelope of ausferrite can be observed experimentally by means of optical microscopy only when the ausferritic transformation has not finished yet.[4] The austenite that does not belong to ausferrite is designated in the RVE as austenite halo, which is ingested by the ausferrite, and it is characterized by low carbon content in comparison with the film and block of austenite.

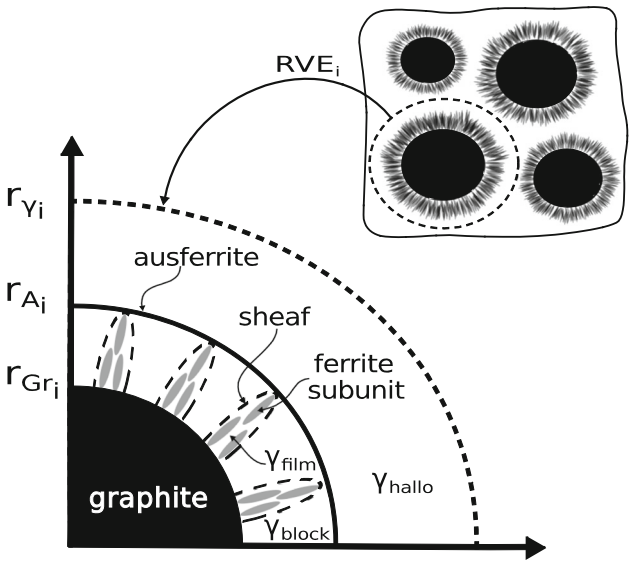

Fig. 1—Representative volume element of a graphite nodule set i, which is proposed to model the ausferritic transformation.

The radii of ausferrite-austenite halo interface and RVE_i interface are denoted as r_{A_i} and r_{γ_i}, respectively. The radius r_{γ_i} is evaluated using the equation:

$$r_{\gamma_i} = \left(\frac{3\mathrm{vol}_{\mathrm{RVE}_i}}{4\pi}\right)^{1/3}, \qquad [3]$$

where $\mathrm{vol}_{\mathrm{RVE}_i} = f_{\mathrm{set}_i}/N_{\mathrm{set}_i}$ is the volume of the RVE_i, f_{set_i} is the normalized graphite volume fraction with respect to the total graphite volume fraction, and N_{set_i} is the number of graphite nodules per unit of volume, all of them for a graphite nodule set i.

The model considers that the subunits are able to grow within ausferrite and at the ausferrite-austenite halo interface. The growth within ausferrite increases the volume fraction of ferrite, while the ausferrite volume fraction remains constant. The growth at the ausferrite-austenite halo interface increases the ausferrite volume fraction, while the ferrite volume fraction remains constant.

B. *Phase Fractions*

The volume fractions of graphite f_{Gr}, ausferrite f_{Ausf}, and ferrite $f_{\alpha\mathrm{p}}$, taking into account the sets of equal size graphite nodules, are evaluated using the following equations:

$$f_{\mathrm{Gr}} = \frac{4\pi}{3}\sum_{i=1}^{\mathrm{nsetsg}} N_{\mathrm{set}_i} r_{\mathrm{Gr}_i}^3, \qquad [4]$$

$$f_{\mathrm{Ausf}} = \frac{4\pi}{3}\sum_{i=1}^{\mathrm{nsetsg}} N_{\mathrm{set}_i}\left(r_{\mathrm{A}_i}^3 - r_{\mathrm{Gr}_i}^3\right), \qquad [5]$$

$$f_{\alpha\mathrm{p}} = \frac{4\pi}{3}\sum_{i=1}^{\mathrm{nsetsg}} f_{\alpha\mathrm{p}_i} N_{\mathrm{set}_i} r_{\gamma_i}^3, \qquad [6]$$

where nsetsg is the sets number of equal size graphite nodules and $f_{\alpha\mathrm{p}_i}$ is the ferrite volume fraction with respect to the RVE_i volume. As in Reference 1, the carbon flux from the metallic matrix to graphite nodule is not considered during the ausferritic transformation; therefore, the graphite nodule radius is assumed to be constant. The volume fraction $f_{\alpha\mathrm{p}_i}$ is evaluated in Section II–D.

The volume fractions of austenite film $f_{\gamma_{\mathrm{film}}}$, austenite block $f_{\gamma_{\mathrm{block}}}$, and austenite halo $f_{\gamma_{\mathrm{halo}}}$, taking into account the sets of equal size graphite nodules, are evaluated using the following equations:

$$f_{\gamma_{\mathrm{film}}} = \frac{4\pi}{3} x_{\gamma\mathrm{f}/\alpha\mathrm{p}} \sum_{i=1}^{\mathrm{nsetsg}} f_{\alpha\mathrm{p}_i} N_{\mathrm{set}_i} r_{\gamma_i}^3, \qquad [7]$$

$$f_{\gamma_{\mathrm{block}}} = \frac{4\pi}{3}\sum_{i=1}^{\mathrm{nsetsg}} \left[N_{\mathrm{set}_i}\left(r_{\mathrm{A}_i}^3 - r_{\mathrm{Gr}_i}^3\right) - f_{\alpha\mathrm{p}_i} N_{\mathrm{set}_i}\left(1 + x_{\gamma\mathrm{f}/\alpha\mathrm{p}}\right) r_{\gamma_i}^3\right], \qquad [8]$$

$$f_{\gamma_{\text{halo}}} = \frac{4\pi}{3} \sum_{i=1}^{\text{nsetsg}} N_{\text{set}_i} \left(r_{\gamma_i}^3 - r_{\text{A}_i}^3 \right), \quad [9]$$

where $x_{\gamma\text{f}/\alpha\text{p}}$ is the ratio between the volume fractions of austenite film and ferrite subunit within a sheaf. This concept is equivalent to the ratio between the volumes of austenite film and ferrite subunit.[19,20] This ratio is assumed constant for all sheaves, and set to $x_{\gamma\text{f}/\alpha\text{p}} = 0.12$.[20]

The total austenite volume fraction f_γ is evaluated as

$$f_\gamma = f_{\gamma_{\text{film}}} + f_{\gamma_{\text{block}}} + f_{\gamma_{\text{halo}}}. \quad [10]$$

The initial graphite and austenite volume fractions are evaluated in this work by considering the carbon mass conservation in all the ductile cast iron. Moreover, the austenite carbon concentration is considered constant in the matrix at the austenitization temperature. The last consideration can be applied if the material has been austenitized during enough time. The initial fractions are

$$f_{\text{Gr}_0} = \left[1 + \frac{\rho_{\text{Gr}}}{\rho_\gamma} \left(\frac{c_{\text{Gr}} - c_{\text{n}}}{c_{\text{n}} - c_\gamma} \right) \right]^{-1}, \quad [11]$$

$$f_{\gamma_0} = 1 - f_{\text{Gr}_0}, \quad [12]$$

where c_{Gr} is the graphite carbon content, c_γ is the austenite carbon concentration at the beginning of the transformation, and c_{n} is the ductile cast iron carbon content. Here and throughout this work, all concentrations are defined in weight percentage (wt pct). The graphite and austenite densities are ρ_{Gr} and ρ_γ, respectively, which are evaluated in Section II–G. The graphite carbon concentration is set to $c_{\text{Gr}} = 100$. The austenite carbon concentration at the beginning of the transformation, which is proposed here with the same value as the equilibrium austenite carbon concentration at the austenite-graphite interface at the austenitization temperature, is evaluated with the equation proposed in Reference 16:

$$c_\gamma = 0.0028(T - 273) + 0.11\text{Mn} - 0.057\text{Si} - 0.058\text{Ni} + 0.13\text{Cu} - 0.12\text{Mo} - 1.7, \quad [13]$$

where the temperature T is measured in K. Additionally, Mn, Si, Ni, Cu, and Mo are the manganese, silicon, nickel, cupper, and molybdenum concentrations in austenite.

C. *Evolution of Ausferrite Volume Fraction*

The evolution of ausferrite volume fraction depends on the growth rate of ausferrite-austenite halo interface. The growth of the ausferrite-austenite halo interface occurs because new subunits nucleate and grow at the tips of sheaves, which is equivalent to new subunits that nucleate and grow at the ausferrite-austenite halo interface. The subunit nucleation and growth is characterized as a discrete process along time and, therefore, the sheaf tip growth is also discrete. By assuming a continuous sheaf tip growth, the evolution of r_{A_i} is

$$\frac{\text{d}r_{A_i}}{\text{d}t} = \frac{l_{\alpha\text{p}}}{t_{\text{gro}} + t_{\text{inc}_i}}, \quad [14]$$

where $l_{\alpha\text{p}} / \left(t_{\text{gro}} + t_{\text{inc}_i} \right)$ is the average radial growth rate of a sheaf tip, in which $l_{\alpha\text{p}}$ is the length of a subunit. Moreover, t_{gro} and t_{inc_i} are the growth time and incubation time, respectively, of a set of subunits that nucleate at the same time. The growth process is considered instantaneous, *i.e.*, $t_{\text{gro}} = 0$ second,[18] and t_{inc_i} is evaluated in Section II–E.

Because there is a void in the literature concerning geometry measurements of ferrite subunits in ductile cast iron, and taking into account that the austempered matrix of ductile cast iron is similar to that of steel, the subunit length, in m, is evaluated as in Reference 18:

$$l_{\alpha\text{p}} = 1 \times 10^{-5} \left(\frac{T - 528}{150} \right). \quad [15]$$

When the ausferrite volume fraction is high, there are contacts between neighboring shells of ausferrite which are growing, as illustrated in Figure 2; therefore, the ausferrite growth rate decreases. This phenomenon has been taken into account with a coefficient which multiplies the right-hand side of Eq. [14] when the shells begin to be in contact[21]:

$$\text{GI} = \left[\frac{1 - (f_{\text{Gr}} + f_{\text{Ausf}})}{1 - f_{\text{con}}} \right]^{2/3}, \quad [16]$$

where f_{con} is the sum of graphite and ausferrite volume fractions when the neighboring shells of the ausferrite begin to be in contact. Following Reference 21, this value has been set to $f_{\text{con}} = 0.5$.

D. *Evolution of Ferrite Volume Fraction*

The evolution of the ferrite volume fraction, with respect to RVE_i, depends on the nucleation and growth within the ausferrite region. The proposed equation to compute the evolution of $f_{\alpha\text{p}_i}$, which has been developed in the same way as the Rees-Bhadeshia's equation for steel,[15] is

$$\frac{\text{d}f_{\alpha\text{p}_i}}{\text{d}t} = \frac{u_{\alpha\text{p}} I_{\alpha\text{p}_i} N_{\alpha\text{ps}_i}}{\text{vol}_{\text{RVE}_i}}, \quad [17]$$

where $u_{\alpha\text{p}}$ is the ferrite volume per subunit, $I_{\alpha\text{p}_i}$ is the number of sets of subunits formed per unit of time, and $N_{\alpha\text{ps}_i}$ is the number of subunits per set of subunits.

Because of the above-mentioned reason about the geometric characterization of a ferrite subunit, the subunit volume, in m^3, is evaluated as in Reference 18:

$$u_{\alpha\text{p}} = 2 \times 10^{-17} \left(\frac{T - 528}{150} \right)^3. \quad [18]$$

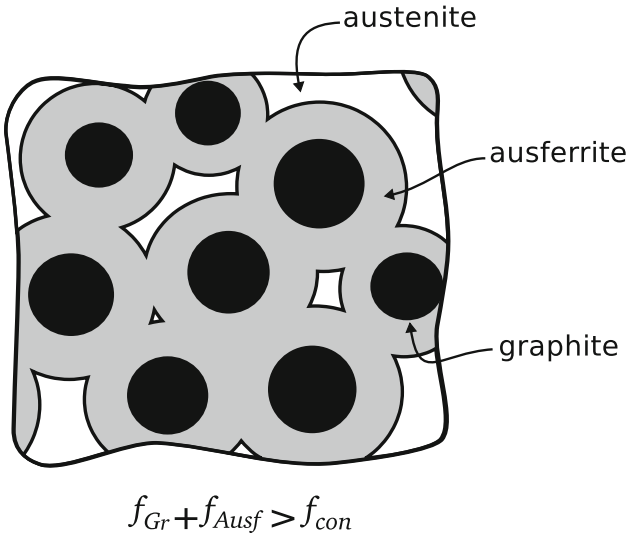

Fig. 2—Contact of neighboring ausferrite shells during the ausferritic transformation.

According to Matsuda-Bhadeshia,[18] the number of sets of subunits formed per unit of time could be related to the incubation time of a set of subunits t_{inc_i} as

$$I_{\alpha\text{p}_i} = \frac{1}{t_{\text{inc}_i}}. \quad [19]$$

The nucleation of ferrite within the ausferrite is modeled using the extended volume concept. The number of subunits per set of subunits is evaluated as

$$N_{\alpha\text{ps}_i} = (1-\xi_i)N^{\text{ext}}_{\alpha\text{ps}_i}, \quad [20]$$

where $N^{\text{ext}}_{\alpha\text{ps}_i}$ is the number of subunits per set of subunits which nucleate into an extended volume, and it is evaluated in Section II–F. Moreover, $\xi_i = f_{\alpha\text{p}_i} \Big/ f_{\alpha\text{p}^{\text{ausf}}_{\text{max}_i}}$ is a coefficient that diminishes $N^{\text{ext}}_{\alpha\text{ps}_i}$ in order to take into account the reduction of nucleation site with the evolution of the ausferritic transformation. The volume fraction $f_{\alpha\text{p}^{\text{ausf}}_{\text{max}_i}}$ represents the fraction of ferrite when the ausferritic transformation stops. For instance, if $f_{\alpha\text{p}_i} = f_{\alpha\text{p}^{\text{ausf}}_{\text{max}_i}}$ ($\xi_i = 1$), the thermodynamic criteria are not satisfied (Eqs. [1] and [2]), and therefore new subunits are not able to nucleate within the ausferrite. The volume fraction $f_{\alpha\text{p}^{\text{ausf}}_{\text{max}_i}}$ is evaluated as

$$f_{\alpha\text{p}^{\text{ausf}}_{\text{max}_i}} = \theta f_{\text{Ausf}_i}, \quad [21]$$

$$\theta = \frac{c_{\gamma_{T_{0'}}}\rho_{\gamma_{T_{0'}}} - c_\gamma \rho_{\gamma_0}}{c_{\gamma_{T_{0'}}}\rho_{\gamma_{T_{0'}}} - c_{\alpha\text{p}}\rho_{\alpha\text{p}}}, \quad [22]$$

where θ is the maximum volume fraction of austenite that is able to transform into ferrite,[9,15] c_γ is the average carbon concentration of austenite prior to the ausferritic transformation, $c_{\alpha\text{p}}$ is the average carbon concentration of a ferrite subunit, ρ_{γ_0} is the austenite density at the beginning of the transformation, $\rho_{\alpha\text{p}}$ is the ferrite density, and $\rho_{\gamma_{T_{0'}}}$ is the austenite density when the ausferritic transformation stops. The densities are evaluated in Section II–G. The ausferrite volume fraction, with respect to RVE$_i$, is $f_{\text{Ausf}_i} = \left(r^3_{A_i} - r^3_{\text{Gr}_i}\right) \Big/ r^3_{\gamma_i}$.

The ferrite carbon concentration, assumed as the upper ferrite subunit, is set to $c_{\alpha\text{p}} = 0.03$,[9] while the austenite carbon concentration, when the ausferritic transformation stops, is evaluated with the equation proposed in Reference 16:

$$c_{\gamma_{T_{0'}}} = 3.072 - 0.0016(T-273) - 0.24\text{Si} - 0.161\text{Mn} - 0.115\text{Ni} + 0.25\text{Cu} + 0.06\text{Mo} + 2.69\text{Cr}, \quad [23]$$

where Cr is the chromium concentration in austenite.

Replacing Eqs. [19] and [20] into [17], the ferrite volume fraction evolution is

$$\frac{\text{d}f_{\alpha\text{p}_i}}{\text{d}t} = (1-\xi_i)\frac{u_{\alpha\text{p}}N^{\text{ext}}_{\alpha\text{ps}_i}}{\text{vol}_{\text{RVE}_i}t_{\text{inc}_i}}. \quad [24]$$

E. *Incubation Time of Subunit Set*

The incubation time of a set of subunits depends on the activation energy G_i for nucleation as[18]

$$t_{\text{inc}_i} \propto \frac{1}{\nu}\exp\left(\frac{G_i}{RT}\right), \quad [25]$$

where ν is the attempt frequency factor defined as $\nu = k_\text{b}T/h$ with k_b and h being the Boltzmann and Planck constants, respectively, and R is the universal gas constant.

If the activation energy for nucleation, independently of the site of nucleation,[22] is considered proportional to the driving force for transformation, the incubation time of a set of subunits can be expressed as[18]

$$t_{\text{inc}_i} = \frac{k_1}{\nu}\exp\left[\frac{k_2}{RT}\left(1+\frac{\Delta G_{\text{m}_i}}{k_3}\right)\right], \quad [26]$$

where ΔG_{m_i} is the maximum free energy available for paraequilibrium nucleation, k_1, k_2, and k_3 are constants, with $k_3 = 2540$ J/mol.[15,18]

Similar to Rees-Bhadeshia,[15] the evaluation of the maximum free energy available for nucleation is proposed as

$$\Delta G_{\text{m}_i} = \Delta G^0_\text{m} - f_{\text{ab}_i}\left(\Delta G^0_\text{m} - G_\text{n}\right), \quad [27]$$

where ΔG^0_m is the maximum free energy available for nucleation when the transformation begins, and f_{ab_i} is a function that allows ΔG_{m_i} to take into account the austenite carbon concentration. Notice that $f_{\text{ab}_i} = 1$ causes that Eq. [1] is not satisfied and, therefore, the nucleation process stops. The value of ΔG^0_m is evaluated using the parallel tangent construction described in Reference 23. The stored energy due to the shape

deformation is set to $G_{sd} = -400$ J/mol.[15] The minimum energy is evaluated, in J/mol, as[15,18,20]

$$G_n = 3.637(T - 273) - 2540. \quad [28]$$

A linear function of the austenite carbon concentration is proposed for f_{ab_i} as

$$f_{ab_i} = \frac{c_{\gamma nz_i} - c_\gamma}{c_{\gamma_{T_{0'}}} - c_\gamma}, \quad [29]$$

where $c_{\gamma nz_i}$ is the carbon concentration of austenite, in which subunits nucleate. For subunits that nucleate within ausferrite, the austenite carbon concentration is assumed as $c_{\gamma nz_i} = c_{\gamma_{block_i}}$. For subunits that nucleate at the ausferrite-austenite halo interface, the austenite carbon concentration is assumed as $c_{\gamma nz_i} = \left(c_{\gamma_{block_i}} + c_{\gamma_{halo}}\right)/2$.

The carbon concentration of austenite halo is assumed as $c_{\gamma_{halo}} = c_\gamma$. The carbon concentration of austenite block is evaluated taking into account the carbon mass conservation within the ausferrite as

$$c_{\gamma_{block_i}} = \frac{f_{Ausf_i} c_\gamma \rho_{\gamma_0} - \left(f_{\alpha p_i} c_{\alpha p} \rho_{\alpha p} + f_{\gamma_{film_i}} c_{\gamma_{film}} \rho_{\gamma_{film}}\right)}{f_{\gamma_{block_i}} \rho_{\gamma_{block_i}}}, \quad [30]$$

where $\rho_{\gamma_{film}}$ and $\rho_{\gamma_{block_i}}$ are the austenite film density and austenite block density for a set i of graphite nodule, respectively, all of them at a transformation time t. The austenite film carbon concentration is assumed as $c_{\gamma_{film}} = c_{\gamma_{T_{0'}}}$.

F. *Number of Ferrite Subunits per Subunit Set*

The subunits, which grow within ausferrite, have two possible nucleation sites. According to experimental observations, subunits could nucleate at graphite nodule surface and at the tips of existing subunits. Nucleation at nodule surface has an important effect in the kinetics of transformation at the beginning of the transformation, because transformation begins in this place. Nucleation at tips of subunits has an important effect in the kinetics of transformation when the number of subunits is high. The proposed equation to take into account the contribution of these two nucleation types is written as

$$N^{ext}_{\alpha ps_i} = N^{ext}_{\alpha ps_{gr_i}} + N^{ext}_{\alpha ps_{tip_i}}, \quad [31]$$

where $N^{ext}_{\alpha ps_{gr_i}}$ and $N^{ext}_{\alpha ps_{tip_i}}$ are the number of subunits per set of subunits related to nucleation at both nodule surface and tips of subunits, respectively.

It is assumed that $N^{ext}_{\alpha ps_{gr_i}}$ has a maximum value when the transformation starts. Then, $N^{ext}_{\alpha ps_{gr_i}}$ decreases because the available nodule surface area decreases. This behavior is modeled by the proposed equation:

$$N^{ext}_{\alpha ps_{gr_i}} = A_i(1 - \varphi_i), \quad [32]$$

where A_i represents the number of subunits in the first subunit set, and $\varphi_i = f_{\alpha p_{gr_i}} \Big/ f_{\alpha p^{max}_{gr_i}}$. The volume fraction $f_{\alpha p_{gr_i}}$ represents the ferrite fraction at time t, and $f_{\alpha p^{max}_{gr_i}}$ is the maximum possible ferrite volume fraction, both of them around the nodule surface; see Figure 3(a). The fraction $f_{\alpha p^{max}_{gr_i}}$ is evaluated as

$$f_{\alpha p^{max}_{gr_i}} = \theta \frac{vol_{Ausf_i^{set_1}}}{vol_{RVE_i}}, \quad [33]$$

where $vol_{Ausf_i^{set_1}} = 4\pi\left[\left(r_{Gr_i} + l_{\alpha p}\right)^3 - r^3_{Gr_i}\right]\Big/3$ is the volume of ausferrite that contains the subunits place around the nodule surface.

The value of A_i is estimated analyzing the first set of subunits; see Figure 3(b). The number of subunits in the first subunit set, which is A_i, is

$$A_i = \frac{vol_{\alpha p_i^{set_1}}}{u_{\alpha p}}, \quad [34]$$

where $vol_{\alpha p_i^{set_1}} = f_{\alpha p_i^{set_1}} vol_{Ausf_i^{set_1}}$ is the ferrite volume of the first set of subunits. The fraction $f_{\alpha p_i^{set_1}}$ represents the ferrite volume fraction of the first set of subunits, with respect to $vol_{Ausf_i^{set_1}}$. Its value is assumed as $f_{\alpha p_i^{set_1}} = \theta$.

The proposed $N^{ext}_{\alpha ps_{tip_i}}$ increases with the number of subunits. This behavior is modeled as

$$N^{ext}_{\alpha ps_{tip_i}} = B n_{\alpha p_i}, \quad [35]$$

where B is the number of new subunits that could be formed per each existing subunit, and $n_{\alpha p_i}$ is the number of existing subunits in which the new set of subunits will nucleate.

The number of new subunits that could be formed per each existing subunit is set to $B = 1$, because it is considered that each subunit has a tip, in which a new subunit could be formed; see Figure 4. The value of $n_{\alpha p_i}$ is considered equal to the total number of subunits within RVE_i at time t as

$$n_{\alpha p_i} = \frac{f_{\alpha p_i} vol_{RVE_i}}{u_{\alpha p}}. \quad [36]$$

G. *Deformation Evolution*

In some occasions, the kinetics of ausferrite transformation is experimentally characterized by the evolution of relative deformation.[4,24] Therefore, a mechanical model is implemented to relate the evolutions of phase and deformation. Considering small deformations, the linear deformation is evaluated by[5,25]

$$\varepsilon = \frac{1}{3}\left(\frac{\rho_0^{mic}}{\rho^{mic}} - 1\right). \quad [37]$$

The densities ρ_0^{mic} and ρ^{mic} are defined as

$$\rho_0^{mic} = f_{Gr_0}\rho_{Gr_0} + f_{\gamma_0}\rho_{\gamma_0}, \quad [38]$$

where f_{Gr_0} and f_{γ_0} are the graphite and austenite volume fractions, respectively, and ρ_{Gr_0} is the graphite

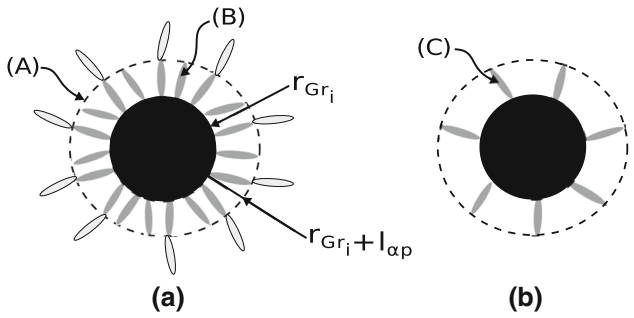

Fig. 3—Nucleation of subunits at nodule surface. (*a*) Nucleation of several sets of subunits and (*b*) nucleation of the first set of subunits. In the figure, *A* represents the ausferrite surface associated to subunits around nodule surface, *B* represents the subunits around nodule surface, and *C* represents the first set of subunits.

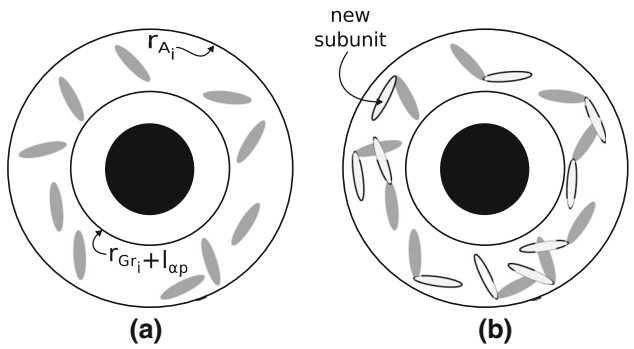

Fig. 4—Nucleation of ferrite subunits at the tips of existing subunits, according to extended volume concept. Interior of ausferrite (*a*) before a new nucleation and (*b*) after a new nucleation.

density, all of them at the beginning of the transformation.

$$\rho^{\text{mic}} = f_{\text{Gr}}\rho_{\text{Gr}} + f_{\alpha p}\rho_{\alpha p} + f_{\gamma_{\text{film}}}\rho_{\gamma_{\text{film}}} + f_{\gamma_{\text{block}}}\rho_{\gamma_{\text{block}}} + f_{\gamma_{\text{halo}}}\rho_{\gamma_{\text{halo}}}, \quad [39]$$

where $\rho_{\gamma_{\text{halo}}}$ and $\rho_{\gamma_{\text{block}}}$ are the austenite halo density and the average austenite block density, respectively, both of them at a transformation time t.

To compute the graphite density, the secant coefficient of thermal expansion of graphite α^{s}_{Gr} is employed:

$$\rho_{\text{Gr}} = \frac{\rho_{\text{Gr}_{\text{amb}}}}{1 + 3\alpha^{s}_{\text{Gr}}(T - T_{\text{amb}})}, \quad [40]$$

where $\rho_{\text{Gr}_{\text{amb}}}$ is the graphite density at ambient temperature T_{amb}, which is set to $\rho_{\text{Gr}_{\text{amb}}} = 2200$ kg/m^3.[26] The coefficient α^{s}_{Gr}, in 1/K, is evaluated as in Reference 27:

$$\alpha^{s}_{\text{Gr}} = 4.06 \times 10^{-6}\left[0.853157 + 4.26564 \times 10^{-4}(T - 273) - 1.42849 \times 10^{-7}(T - 273)^2\right]. \quad [41]$$

The ferrite subunit, austenite film, austenite block, and austenite halo densities, in kg/m^3, are computed as in Reference 28:

$$\rho_{\alpha p} = 7875.96 - 0.297(T - 273) - 5.62 \times 10^{-5}(T - 273)^2 + \left[-206.35 + 0.00778(T - 273) + 1.472 \times 10^{-6}(T - 273)^2\right] C_{\alpha p} + \left[-8.58 + 1.229 \times 10^{-3}(T - 273) + 0.852 \times 10^{-7}(T - 273)^2 + 0.018367\text{Cr}_{\alpha p}\right] \text{Cr}_{\alpha p} + \left[-0.22 - 0.47 \times 10^{-3}(T - 273) - 1.855 \times 10^{-7}(T - 273)^2 + 0.104608\text{Ni}_{\alpha p}\right] \text{Ni}_{\alpha p} - 36.86\text{Si}_{\alpha p} - 7.24\text{Mn}_{\alpha p} + 30.78\text{Mo}_{\alpha p} \quad [42]$$

$$\rho_{\gamma_j} = 8099.79 - 0.506(T - 273) + [-118.26 + 0.00739(T - 273)]C_{\gamma_j} + \left[-7.59 + 3.422 \times 10^{-3}(T - 273) - 5.388 \times 10^{-7}(T - 273)^2 - 0.014271\text{Cr}_{\gamma_j}\right] \text{Cr}_{\gamma_j}, + \left[1.54 - 2.267 \times 10^{-3}(T - 273) - 11.26 \times 10^{-7}(T - 273)^2 + 0.062642\text{Ni}_{\gamma_j}\right] \text{Ni}_{\gamma_j} - 68.24\text{Si}_{\gamma_j} - 6.01\text{Mn}_{\gamma_j} + 12.45\text{Mo}_{\gamma_j} \quad [43]$$

where C is the carbon concentration, and the subscript j stands for 0, T_0, film, block, and halo.

H. *Numerical Implementation*

This model was implemented computationally using the software Octave. A flow diagram of the proposed algorithm is presented in Figure 5.

The required input is chemical composition, austenitization and austempering temperatures, austempering time (t_s), sets number of equal size graphite nodules, number of graphite nodules per unit of volume, and the fitted constants k_1 and k_2.

The model needs initial information that depends on the input data, which is calculated in the initial data block. This information is composed by phase carbon concentrations, phase densities, initial phase fractions, size of ferrite subunit, maximum free energy available for nucleation when the transformation begins, and minimum energy necessary to obtain a detectable amount of ferrite.

The ordinary differential equations for ausferrite and ferrite growths (Eqs. [14] and [24], respectively) are solved sequentially by the one-step Euler's numerical method.[29] For each time increment Δt, the phase fractions and deformation are calculated; moreover, all the variables are updated.

Finally, when $t \geq t_s$, the simulation is interrupted and the output files containing the evolution of phase fractions, austenite carbon concentrations, and deformation are generated.

III. CASES STUDIED

The proposed model has been used in this research to reproduce the experimental results reported in References 4, 5, and 24. It is possible to use those experiments to validate the model, because there is no evidence of reconstructive transformation at the end of heat treatment; this is due to the small dimension of coupons (the biggest specimen is a cylinder of diameter 8 mm and length 12 mm), chemical composition, and high cooling rate from austenitization temperature to austempering temperature (25 K/s). It is assumed that ausferritic transformation begins at the same time in all the volume of each specimen; therefore, the experimental measurements are representative of phase evolution in the whole specimen.

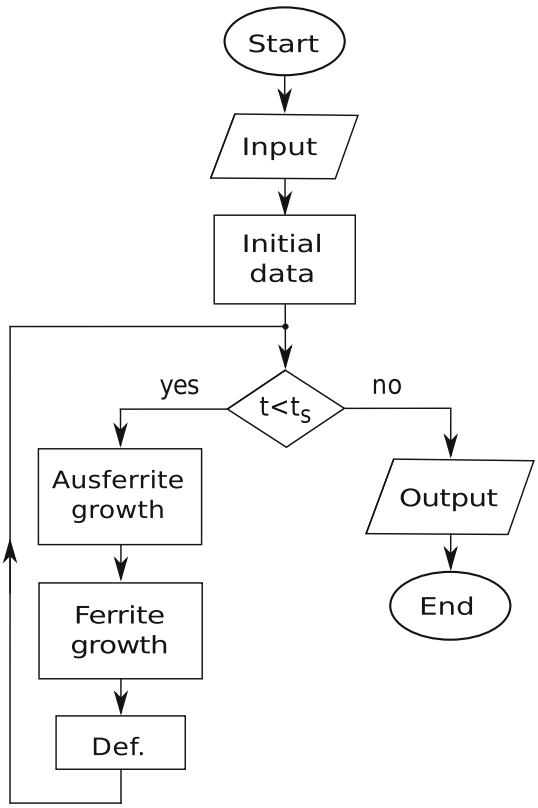

Fig. 5—Flow diagram of the proposed model.

The chemical compositions of the ductile cast irons are shown in Table I. Coupons made of DCI1 have different graphite nodule counts, and austenitization and austempering temperatures, which are presented in Table II. All of them are austenitized between 2400 and 3000 seconds. Coupons made of DCI2 have a graphite nodule count equal to 64×10^6 nodule/m^2. The samples are austenitized 900 seconds at 1223 K (950 °C) and austemperized at different temperatures as shown in Table III.

The graphite nodule count has been characterized in terms of graphite nodules per unit area. The characterized parameter is related to the number of nodules per unit volume as

$$N_{\text{set}_i} = \frac{3}{4}\left(\frac{\pi \text{Na}_{\text{set}_i}^3}{f_{\text{set}_i}}\right)^{1/2}, \qquad [44]$$

where Na_{set_i} is the number of nodules per unit area of a graphite nodule set i. For each modeled coupon, the graphite nodules are grouped into one graphite nodule set (nsetsg = 1 and $f_{\text{set}_1} = 1$).

For each chemical composition, the constants $k_1$and k_2 are obtained by fitting the model response to the experimental results. In order to do that, the heat

Table I. Chemical Position of Ductile Cast Irons[4,5,24]

Ductile Cast Iron	Chemical Composition (wt pct)
DCI1	Fe-3.7C-2.7Si-0.1Mn-0.03Mg
DCI2	Fe-3.55C-2.5Si-0.55Mn-0.15-Mo-0.31Cu-0.042Mg

Table III. Austempering Temperature for Coupons Made of DCI2[24]

Coupon	Austempering Temperature [K (°C)]
1DCI2	573 (300)
2DCI2	623 (350)
3DCI2	653 (380)
4DCI2	673 (400)

Table IV. Constants k_1 and k_2 Obtained by Fitting for DCI1 and DCI2

Ductile Cast Iron	k_1	k_2 (J/mol)
DCI1	1.33×10^{15}	4.7×10^3
DCI2	1.15×10^{15}	12×10^3

Table II. Graphite Nodule Counts, and Austenitization and Austempering Temperatures for Coupons Made of DCI1[4,5]

Coupon	Graphite Nodule Count [1×10^6 nodule/m^2]	Austenitization Temperature [K (°C)]	Austempering Temperature [K (°C)]
1DCI1	140	1193 (900)	673 (400)
2DCI1	330	1193 (920)	673 (400)
3DCI1	840	1173 (900)	673 (400)
4DCI1	1992	1193 (920)	673 (400)
5DCI1	1992	1193 (920)	623 (350)
6DCI1	1992	1193 (920)	573 (300)

treatments of two or three specimens are simulated for different combinations of $k_1$and k_2. The optimal combination minimizes the sum of square difference between numerical and experimental results. The sum takes into account the mentioned difference of all the specimens used in the fitting process for a chemical composition. For chemical composition DCI1, the considered coupons are 2DCI1, 4DCI1, and 6DCI1, because they have different graphite nodule counts and are treated at different austempering temperatures. For DCI2, the coupons are 1DCI2 and 4DCI2 because they are treated at different austempering temperatures. The obtained constants are shown in Table IV.

To evaluate the response of the model to different distributions of graphite nodule size, three virtual specimens with two graphite nodule sets (nsetsg = 2) are proposed by this work. The specimens have a chemical composition equal to DCI1. The graphite nodule count of sets 1 and 2 are $N_{set_1} = 82.5 \times 10^6$ and $N_{set_2} = 247.5 \times 10^6$ nodule/m^2 (total graphite nodule count is equal to 330×10^6 nodule/m^2). Different sizes of graphite nodule are obtained by different normalized graphite volume fractions, as are shown in Table V. The coupons are austenitized and austempered at 1193 K and 673 K (920 °C and 400 °C), respectively.

IV. RESULTS AND DISCUSSION

The computed normalized expansions, corresponding to the specimens used in the fitting process for DCI1, are presented in Figure 6. The comparison of curves corresponding to 4DCI1 [673 K (400 °C)] and 6DCI1 [573 K (300 °C)] illustrates the effect of austempering temperature, whereas the effect of graphite nodule count is observed by comparison of curves corresponding to 2DCI1 (330×10^6 nodule/m^2) and 4DCI1 (1992×10^6 nodule/m^2). A difference with available models in the literature is that the present model is able to represent the influence of austempering temperature and graphite nodule count using the same value of $k_1$and k_2, for each chemical composition.

The computed evolution of the phases during the ausferritic transformation is shown in Figure 7. The ferrite evolution has a sigmoidal behavior, as observed in experimental reports.[4,24] The fraction of austenite halo tends to zero; meanwhile, the ausferrite tends to the matrix fraction. This opposite behavior occurs because ausferrite ingests austenite halo. The fraction of austenite block increases up to a maximum, and then decreases up to its final fraction. The kinetics of austenite block depends on the ausferrite growth, which increases the austenite block fraction, and the ferrite growth which decreases the austenite block fraction. The described behavior occurs because the contributions of these two growths change during the transformation.

Table V. Proposed Normalized Graphite Volume Fraction for Sets 1 and 2

Coupon	f_{set_1}	f_{set_2}
P1DCI1	0.25	0.75
P2DCI1	0.5	0.5
P3DCI1	0.7	0.3

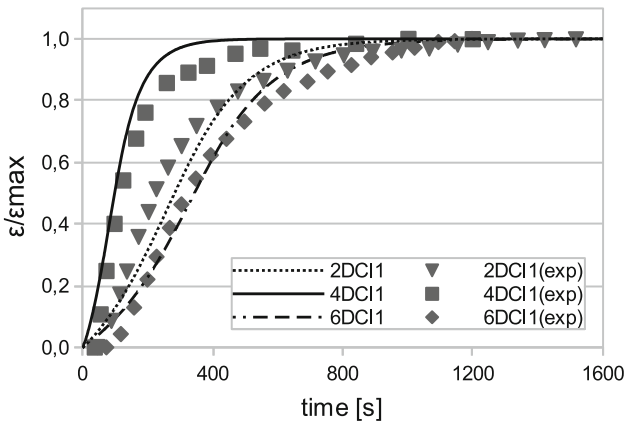

Fig. 6—Computed normalized expansions.

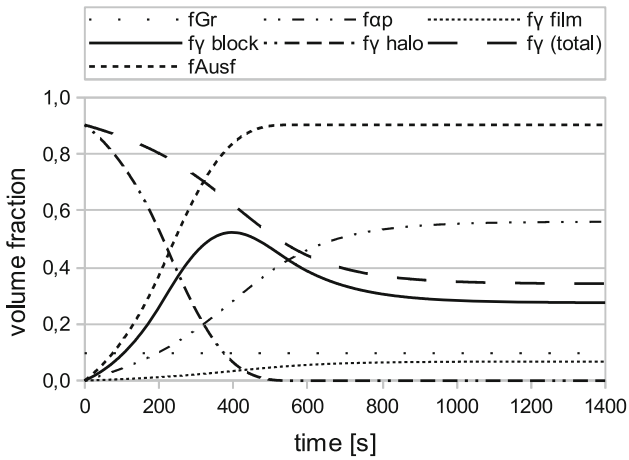

Fig. 7—Computed evolution of volume fractions during the austempering transformation for coupon 1DCI1.

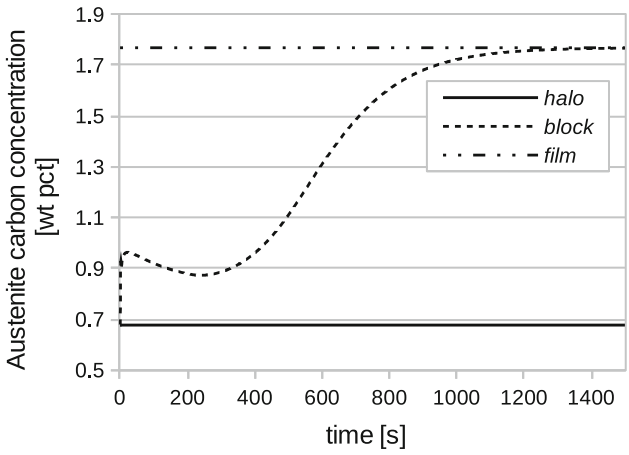

Fig. 8—Computed evolution of carbon concentration in the three regions of austenite during the austempering transformation for coupon 1DCI1.

The evolution of the austenite carbon concentration, during the transformation, is observed in Figure 8. The carbon concentrations of austenite film and austenite halo remain constant, as proposed by the model. Initially, the carbon concentration of austenite block is equal to the austenite halo carbon concentration and, when the transformation stops, it is equal to the austenite film carbon concentration. Its evolution is characterized by a rapid increment when the transformation starts and by a sigmoidal behavior after 250 seconds. The observed minimum value (close to 250 seconds) is related to the rapid growth of austenite block between 200 and 300 seconds.

The influence of graphite nodule count in the kinetics of ausferritic transformation can be observed in Figure 9: when the graphite nodule count increases, the transformation rate also increases. The contribution of nucleation at the graphite nodule surface, to the final ferrite fraction, increases in ductile cast iron with high nodule counts. In a hypothetical case in which the ductile cast iron has a very high number of graphite nodules, there is no contribution of nucleation at the tips of the existing subunits. The transformation rates, related to both nucleation regions, are different; this explains the influence of different graphite nodule counts in the kinetics. On the other hand, the difference between the final ferrite fractions corresponds to different austenitization temperatures. The highest fraction correspond to 1173 K (900 °C) and the lowest to 1193 K (920 °C). The ferrite fraction increases with a temperature decrement, because the initial austenite carbon concentration decreases, as stated by Eq. [13]. The same response was obtained by experimental tests in Reference 30.

The influence of austempering temperature in the kinetics of ausferritic transformation is depicted in Figure 10. With a temperature increment, the transformation rate increases. This behavior occurs because the incubation time of a subunit set decreases and the subunit size increases, both of them with a temperature increment. The final ferrite fraction increases with a temperature decrement, because the austenite carbon concentration at the end of the ausferritic transformation increases, as stated by Eq. [23]. The same response was obtained by experimental test in Reference 9.

Figure 11 shows the effect of different distributions of graphite nodule size in the ausferritic transformation. In all cases, the evolution preserves the sigmoidal behavior. In specimen P3DCI1, which has the maximum difference in graphite nodule size (9×10^{-6} and 23.8×10^{-6} m), the contributions to the ferrite kinetics of sets 1 and 2 can be identified. According to this case, a small increment of the required time to complete the ausferritic transformation is obtained when the difference in the graphite nodule size increases.

The comparison between numerical and experimental austenite volume fraction at the end of the heat treatment, for coupons made of DCI2, is presented in Figure 12. The numerical results are in good agreement with experiments. An increment of austenite volume fraction with an increment of austempering temperature is observed.

Figures 13 and 14 show the influence of austempering temperature on the required time to complete the ausferritic transformation for coupons made of DCI1

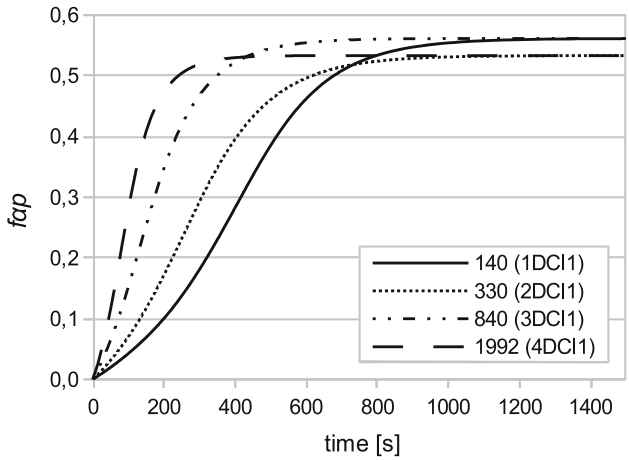

Fig. 9—Computed evolution of ferrite volume fraction for different graphite nodule counts.

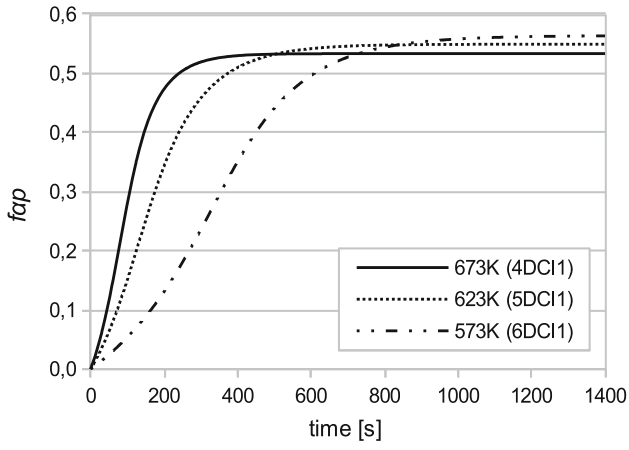

Fig. 10—Computed evolution of ferrite volume fraction for different austempering temperatures.

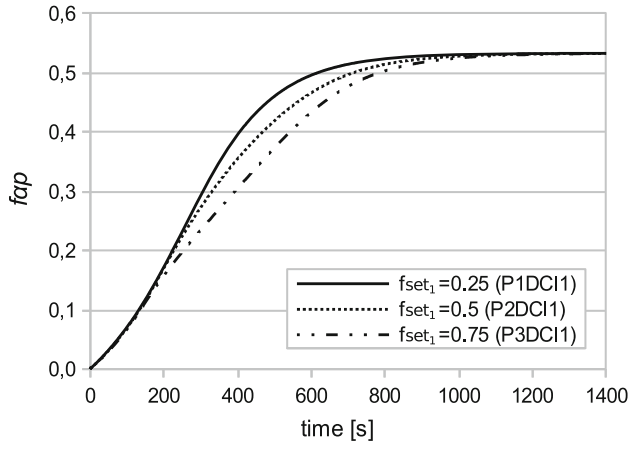

Fig. 11—Computed evolution of ferrite volume fraction for different distributions of graphite nodule size.

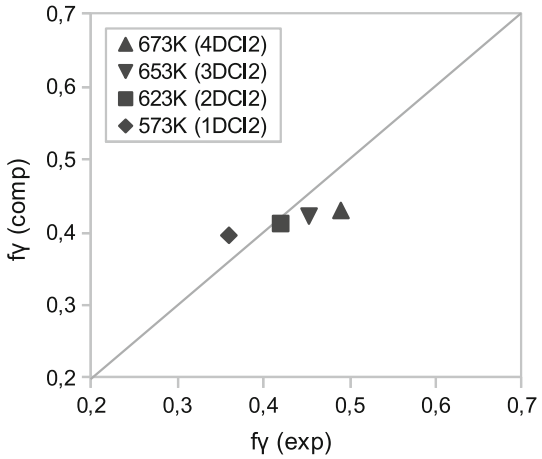

Fig. 12—Comparison between computed and experimental austenite volume fraction, at the end of heat treatment, for coupons made of DCI2.

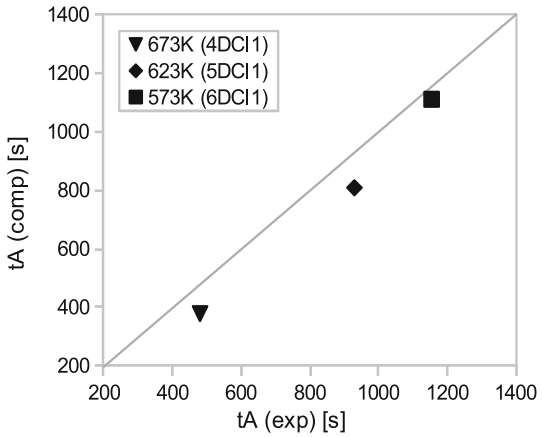

Fig. 13—Required time to complete the ausferritic transformation: influence of austempering temperature in coupons made of DCI1, with 1992×10^6 nodule/m^2 graphite nodule count.

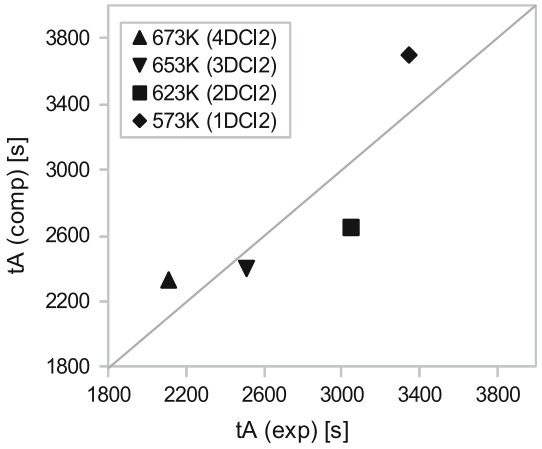

Fig. 14—Required time to complete the ausferritic transformation: influence of austempering temperature in coupons made of DCI2, with 64×10^6 nodule/m^2 graphite nodule count.

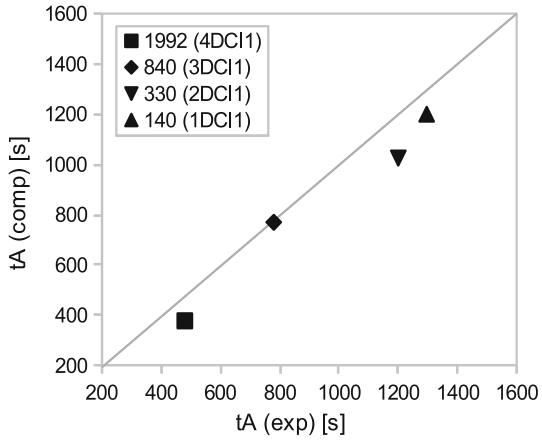

Fig. 15—Required time to complete the ausferritic transformation: influence of graphite nodule count in coupons made of DCI1, austempered at 673 K (400 °C).

and DCI2, respectively. In both cases the increment of the required time, with a decrement of austempering temperature, is well represented. The required times for DCI2 are higher than for DCI1, because its graphite nodule count is considerably higher than in DCI1 (1992×10^6 and 64×10^6 nodule/m^2, respectively). These cases show that the proposed model is able to predict a very important heat treatment parameter for the industry, considering different chemical compositions and austempering temperatures. The austempering temperature is a parameter used to obtain the required microstructure (amount and type of ferrite subunits).

Figure 15 shows the influence of graphite nodule count in the required time to complete the ausferritic transformation for coupons made of DCI1. The increment of the required time, with a decrease of graphite nodule count, is well represented. With the development of thin wall ductile iron, the range of graphite nodule count in commercial materials has been greatly expanded. This case shows that the proposed model is able to predict the effect of this parameter in the required time to complete the modeled transformation, a fact that is important to the industry.

V. CONCLUSIONS

During the production of ADI, a crucial stage is associated with an ausferritic transformation which is responsible for the formation of its characteristic microstructure. There are several models that allow to predicting some aspects of this transformation, but do not take into account the influence of the microstructure characteristics; therefore, they need to be fitted using a large number of experimental results.

A microscale model has been presented in this paper to simulate the evolution of phases during the austempering transformation of ductile cast iron. This model was developed taking into account the displacive mechanism growth and considering the next microstructure

characteristics: graphite nodule count, distribution of graphite nodule size, ferrite subunit size, distribution of phases within the microstructure, and inhomogeneous redistribution of austenite carbon content. Additionally, parameters such as chemical composition, and austenitization and austempering temperatures have also been considered.

In comparison with previous models, only few experimental results are required, for each chemical composition, to fit the proposed model to consider the effect of graphite nodule count and austempering temperature on the kinetics of the ausferritic transformation. After an appropriate fit of the parameters, the data from experimental heat treatments published in the literature were correctly reproduced.

The main conclusions of this study may be summarized as follows:

1. The transformation rate was greatly modified by the graphite nodule count and the austempering temperature, whereas a small influence of different distributions of graphite nodule size was found.
2. The required time to finish the austempering transformation in ductile cast iron increases with low nodule count and/or if it is treated at low austempering temperature. The shortest required time is obtained with the highest graphite nodule count and highest austempering temperature.
3. For a given chemical composition, the final ferrite volume fraction was modified only by the austenitization and austempering temperatures, as has been reported from experiments. The ferrite fraction increases with a decrease of austenitization and/or austempering temperatures. The highest fraction is obtained with the lowest austenitization and austempering temperatures.

ACKNOWLEDGMENTS

Adrián D. Boccardo had a doctoral scholarship from CONICET during this research. Patricia M. Dardati was supported by a grant from UTN. Diego J. Celentano gratefully acknowledges the support of Fondecyt Project 1130404. Luis A. Godoy is a member of the research staff of CONICET.

REFERENCES

1. W. Kapturkiewicz, A.A. Burbelko, J. Lelito, and E. Fraś: *Int. J. Cast Met. Res.*, 2003, vol. 16 (1–3), pp. 287–92.
2. B.V. Kovacs: *AFS Trans.*, 1994, vol. 83, pp. 417–20.
3. S.M. Yoo, K. Moeinipour, A. Ludwig, and P.R. Sahm: *Int. J. Cast Met. Res.*, 1999, vol. 11, pp. 483–88.
4. E. Fraś, M. Górny, E. Tyrała, and H. Lopez: *Mater. Sci. Technol.*, 2012, vol. 28, pp. 1391–96.
5. A.D. Boccardo, P.M. Dardati, D.J. Celentano, L.A. Godoy, M. Górny, and E. Tyrała: *Mater. Trans. B*, 2015, vol. 47, pp. 566–75.
6. R.C. Thomson, J.S. James, and D.C. Putman: *Mater. Sci. Technol.*, 2000, vol. 16, pp. 1412–19.
7. D.C. Putman and R.C. Thomson: *Int. J. Cast Met. Res.*, 2003, vol. 16 (1–3), pp. 191–96.
8. S. Mendez, U. de la Torre, P. Larranaga, R. Suarez, and D.M. Stefanescu: *Met. Cast. Des. Purch.*, 2015, vol. 17 (5), pp. 39–44.
9. M.A. Yescas and H.K.D.H. Bhadeshia: *Mater. Sci. Eng. A*, 2002, vol. 333, pp. 60–66.
10. L. Meier, M. Hofmann, P. Saal, W. Volk, and H. Hoffmann: *Mater. Charact.*, 2013, vol. 85, pp. 124–33.
11. B. Bosnjak, B. Radulovic, K. Pop-Tonev, and V. Asanovic: *J. Mater. Eng. Perform.*, 2001, vol. 10 (2), pp. 203–11.
12. U. Batra, S. Ray, and S.R. Prabhakar: *J. Mater. Eng. Perform.*, 2004, vol. 13 (1), pp. 64–68.
13. M. Górny, E. Tyrała, and H. Lopez: *J. Mater. Eng. Perform.*, 2014, vol. 23 (10), pp. 3505–10.
14. H.K.D.H. Bhadeshia: *Bainite in Steels*, 2nd ed., IOM Communications Ltd., London, 2001, pp. 129–88.
15. G.I. Rees and H.K.D.H. Bhadeshia: *Mater. Sci. Technol.*, 1992, vol. 8, pp. 985–93.
16. L.C. Chang: *Metall. Mater. Trans. A*, 2003, vol. 34A, pp. 211–17.
17. Z. Ławrynowicz: *Adv. Mater. Sci.*, 2016, vol. 16 (2), pp. 47–56.
18. H. Matsuda and H.K.D.H. Bhadeshia: *Proc. R. Soc. Lond. A*, 2004, vol. 460, pp. 1707–22.
19. G.I. Rees and H.K.D.H. Bhadeshia: *Mater. Sci. Technol.*, 1992, vol. 8, pp. 994–96.
20. D. Gaude-Fugarolas and P.J. Jacques: *ISIJ Int.*, 2006, vol. 46 (5), pp. 712–17.
21. K. Su, I. Ohnaka, I. Yamauchi, and T. Fukusako: *Mater. Res. Soc. Symp. Proc.*, 1985, vol. 34, pp. 181–89.
22. M.J. Santofimia, F.G. Caballero, C. Capdevila, C. García-Mateo, and C. García de Andrés: *Mater. Trans.*, 2006, vol. 47 (10), pp. 2465–72.
23. H.K.D.H. Bhadeshia: *Metal Sci.*, 1982, vol. 16, pp. 159–65.
24. M.A. Yescas. Modelling the Microstructure and Mechanical Properties of Austempered Ductile Irons, Ph.D. Thesis, University of Cambridge, Cambridge, 2001.
25. F. Christien, M.T.F. Telling, and K.S. Knight: *Mater. Charact.*, 2013, vol. 82, pp. 50–57.
26. J. Lacaze and V. Gerval: *ISIJ Int.*, 1998, vol. 38 (7), pp. 714–22.
27. D.K.L. Tsang, B.J. Marsden, S.L. Fok, and G. Hall: *Carbon*, 2005, vol. 43, pp. 2902–06.
28. J. Miettinen: *Metall. Mater. Trans. B*, 1997, vol. 28B, pp. 281–97.
29. S.C. Chapra and R.P. Canale: *Numerical Methods for Engineers*, 6th ed., McGraw-Hill, New York, 2010, pp. 708–19.
30. U. Batra, S. Ray, and S. Prabhakar: *J. Mater. Eng. Perform.*, 2007, vol. 16 (4), pp. 485–89.